Supporting Information: Understanding Electrolyte Filling of Lithium-Ion Battery Electrodes on the Pore Scale Using the Lattice Boltzmann Method

Martin P. Lautenschlaeger[a,b,*], Benedikt Prifling[c], Benjamin Kellers[a,b], Julius Weinmiller[a,b], Timo Danner[a,b], Volker Schmidt[c], Arnulf Latz[a,b,d]

[a] *German Aerospace Center (DLR), Institute of Engineering Thermodynamics, 70569 Stuttgart, Germany*
[b] *Helmholtz Institute Ulm for Electrochemical Energy Storage (HIU), 89081 Ulm, Germany*
[c] *Ulm University (UUlm), Institute of Stochastics, 89081 Ulm, Germany*
[d] *Ulm University (UUlm), Institute of Electrochemistry, 89081 Ulm, Germany*

In the present paper, electrolyte filling processes were studied by means of the lattice Boltzmann method (LBM) with regard to the influence of structural and physico-chemical properties as well as the process time t_P. In particular, the influencing factors were the particle size distribution R_PS, the volume fraction ϕ_A, and the wettability θ_A of the active material as well as the the inner volume fraction ϕ'_B and the wettability θ_B of the binder. Results were reported as pressure-saturation relationship, final degree of saturation, detailed analysis of the gas entrapment, and permeability. The numerical values of the results as well as complementary information are given in the following.

The Supporting Information is organized as follows. In Section SI-1 the general LBM and the multi-component Shan-Chen pseudopotential method (MCSC) are briefly described. A verification of the combined MCSC and grayscale (GS) model is given in Section SI-2. The uncertainty estimation of the pressure-saturation curves is described in Section SI-3. The numerical values of the results presented in the present paper are summarized in Section SI-4. Finally, additional plots of the size distributions of gas agglomerates for all simulations from the present paper are shown in Section SI-5.

*Corresponding author:
Email address: Martin.Lautenschlaeger@dlr.de (Martin P. Lautenschlaeger)

SI-1. LBM

SI-1.1. General introduction

The book *The Lattice Boltzmann Method* [1] introduces LBM in very detail. It is also helpful to get a comprehensive overview over the method and its applications. In the following, only a condensed overview of the lattice Boltzmann models that are relevant for the present paper is given.

The general LBM for single-phase fluid flow solves the discretized Boltzmann equation

$$\frac{\partial f_i\left(\mathbf{x},t\right)}{\partial t}+\mathbf{c}_i\nabla f_i\left(\mathbf{x},t\right)=\Omega_i\left(\mathbf{x},t\right), \tag{SI.1}$$

where $\boldsymbol{f}$ are the distribution functions, Ω is a general collision operator, and $\boldsymbol{x}$ and t denote the position of the lattice cell and the time, respectively. As already described in the main text and the appendix of the present paper, Eq. (SI.1) is discretized on a regular and cubic 3D lattice using the D3Q19 velocity set. The directions of the velocity set are denoted as i. They correspond to the directions along which information from the distribution functions $\boldsymbol{f}$ is transferred. They are directly connected to the predefined lattice velocity $\boldsymbol{c}_i$, i.e. the microscopic speed of transport during a single time step Δt. The collision operator Ω describes the physics of the problem via particle collisions which lead to modifications and a redistribution of $\boldsymbol{f}$. The simplest and most commonly used functional form of Ω is from Bhatnagar, Gross, and Krook (BGK) [2]

$$\Omega_i=-\frac{1}{\tilde{\tau}}\left(f_i-f_i^{\mathrm{eq}}\right). \tag{SI.2}$$

The combination of Eqs. (SI.1) & (SI.2) is referred to as the lattice BGK (LBGK) equation. It describes the relaxation of $\boldsymbol{f}$ towards the Maxwell–Boltzmann equilibrium distribution function $\boldsymbol{f}^{\mathrm{eq}}$ (cf. appendix of the present paper). The characteristic relaxation time is denoted by $\tilde{\tau}$.

By solving Eq. (SI.1), different relevant macroscopic properties can be determined locally as moments of $\boldsymbol{f}$. Examples are given in the appendix of the present paper.

In addition, it is also important to model interaction between the fluid and the solid wall since fluid flow through porous electrode structures is studied in the present paper. The simplest and most popular approach for such a no-slip boundary condition is the

bounce-back method [3, 4]. Using this method, distribution functions that approach the wall are reflected back to the lattice cell from which they originated. There are different types of bounce-back schemes reported in the LBM literature, where the so-called halfway bounce-back scheme is applied here [1]. This frequently used approach is defined as

$$f_i(\mathbf{x}, t) = f_{\bar{i}}(\mathbf{x}, t + \Delta t), \tag{SI.3}$$

where $\bar{i}$ denotes the direction opposite to i, i.e. $\boldsymbol{c}_{\bar{i}} = -\boldsymbol{c}_i$.

SI-1.2. Multi-Component Shan-Chen Pseudopotential Method

The MCSC [5] can be applied to study multi-phase fluid flows. It is based on a bottom-up modeling approach [4, 6] in which molecular interaction forces are determined from the pseudopotential $\psi = f(\rho)$. In the following, the model is described for two immiscible components and the pseudopotential $\psi = \rho$, which is a typical choice in the literature [7–12].

In the MCSC, each lattice cell is occupied by all immiscible components. The temporal evolution of $\boldsymbol{f}^\sigma$ is described by the lattice Boltzmann (LB) equation (cf. Eq. (SI.1)) with the BGK collision operator (cf. Eq. (SI.2)). Using the Shan-Chen forcing approach, one obtains

$$f_i^\sigma\left(\mathbf{x} + \mathbf{c}_i \Delta t, t + \Delta t\right) - f_i^\sigma\left(\mathbf{x}, t\right) = -\frac{\Delta t}{\tilde{\tau}^\sigma}\left(f_i^\sigma\left(\mathbf{x}, t\right) - f_i^{\mathrm{eq},\sigma}\left(\mathbf{x}, t\right)\right), \tag{SI.4}$$

where σ denotes the component, i.e. electrolyte or gas phase.

In addition, the interfacial tension between the components σ and $\bar{\sigma}$ is modeled as a fluid-fluid interaction force $\boldsymbol{F}^\sigma_{\mathrm{inter}}$. The wettability or adhesion at a solid wall is modeled as a solid-fluid interaction force $\boldsymbol{F}^\sigma_{\mathrm{ads}}$. The external force fields $\boldsymbol{F}^\sigma_{\mathrm{ext}}$ can be considered in the simulations, where the definition of all three forces is given in the main text. The sum of the aforementioned force contributions determines the total force $\boldsymbol{F}^\sigma_{\mathrm{tot}} = \boldsymbol{F}^\sigma_{\mathrm{inter}} + \boldsymbol{F}^\sigma_{\mathrm{ads}} + \boldsymbol{F}^\sigma_{\mathrm{ext}}$ acting on a lattice cell. Using the Shan-Chen forcing approach [1], $\boldsymbol{F}^\sigma_{\mathrm{tot}}$ is finally incorporated into MCSC as a force-induced contribution to the equilibrium velocity of each component. More precisely, it holds

$$\mathbf{u}^{\mathrm{eq},\sigma} = \frac{\sum_\sigma \rho^\sigma \mathbf{u}^\sigma / \tilde{\tau}^\sigma}{\sum_\sigma \rho^\sigma / \tilde{\tau}^\sigma} + \frac{\tilde{\tau}^\sigma \boldsymbol{F}^\sigma_{\mathrm{tot}}}{\rho^\sigma}. \tag{SI.5}$$

The equilibrium velocity $\boldsymbol{u}^{\mathrm{eq},\sigma}$ must not be confused with the macroscopic streaming velocity of the mixture. The latter has also to be force-corrected and is given by

$$\mathbf{u}_{\mathrm{macro}} = \sum_{\sigma} \left(\sum_{i} \frac{f_i^{\sigma} \mathbf{c}_i}{\rho^{\sigma}} + \frac{\boldsymbol{F}_{\mathrm{tot}}^{\sigma} \Delta t}{2\rho^{\sigma}} \right). \tag{SI.6}$$

SI-2. Verification of Model Parameters

The LB model that was applied for the current study is described in Section 2.1 in the present paper. Compared to the model proposed by Pereira [11, 13, 14] it contains some adaptions and uses a different forcing scheme. Therefore, potential effects of the model changes on the physical behavior of the model were tested. Verifications with respect to the interfacial tension and the wetting behavior were conducted. They are described in the following.

SI-2.1. Interfacial Tension

Fluid flow through a homogenized binder region should not affect the interfacial tension between the electrolyte and the gas phase. Thus, it has to be ensured that setting the same value for $G_{\mathrm{inter}}^{\mathrm{EG}}$ in all lattice cells of the system does not lead to different interfacial tensions.

Therefore, a series of bubble tests was conducted from which the Laplace pressure was determined. The simulation setup is shown in Figure SI-1 and consists of a fully periodic 2D system with a size of 100 cells along the x- and y-direction. The system contains a gas bubble with the density ρ^{G} which is surrounded by electrolyte with the density ρ^{E}. Both components have equal masses. The model parameters were similar to those given in Table 1 in the present paper. Here, in each cell, the homogenized model, i.e. the combined MCSC and GS method, was applied. The values of the solid-fluid interaction parameter $G_{\mathrm{ads}} = G_{\mathrm{ads}}^{\mathrm{G}} = -G_{\mathrm{ads}}^{\mathrm{E}}$ and the solid fraction n_s were were identical in each cell. They were varied between the simulations.

A simulation run consisted of 500,000 time steps in which the pressure difference between the gas bubble and the electrolyte $\Delta p = p^{\mathrm{G}} - p^{\mathrm{E}}$ as well as the bubble radius R were determined every 10,000 time steps. Therefrom, the interfacial tension γ was determined using Laplace's law $\gamma = \Delta p R$.

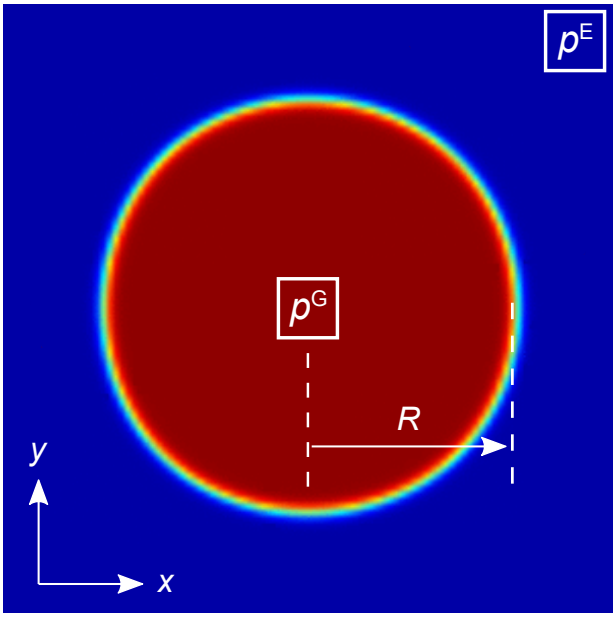

Figure SI-1: Simulation setup for evaluating the influence of the homogenized model on the interfacial tension. A gas bubble (red) with radius R is submersed in an electrolyte phase (blue) of equal mass. The pressures of both the gas phase p^{G} and the electrolyte p^{E} are determined at the locations indicated by the white boxes.

The results are given in Table SI-1. It can be shown that there is no influence of G_{ads} and hardly any impact of n_s on γ. The values of γ are in good agreement with the value of γ used in this study (cf. Table 1 in the present paper). Therefrom, it is concluded that the model adaptions for homogenized components, i.e. $n_s \neq 0$, do not lead to different interfacial tensions compared to the pure MCSC (cf. [8]). Another advantage of the present model is that the scaling of the interfacial force parameter G_{inter} also ensures a stable and non-diverging interface (cf. Figure SI-1).

SI-2.2. Wetting Behavior

The inner volume fraction of the binder $\phi'_{\mathrm{B}} = n_s$ should not affect the contact angle θ between the binder and the electrolyte or the gas, respectively. Thus, it has to be ensured that the choice of the solid-fluid interaction parameter $G_{\mathrm{ads}} = G^{\mathrm{G}}_{\mathrm{ads}} = -G^{\mathrm{E}}_{\mathrm{ads}}$ which determines θ, is independent of n_s.

Typically, the correlation between the solid-fluid interaction force G_{ads} and the contact angle θ is determined via contact angle measurements on solid surfaces. This is not possible when using solids with inner porosity, where the fluid is either fully repelled or

Table SI-1: Results of the surface tensions γ determined from the bubble test simulations. The parameter n_s is the solid fraction of the homogenized lattice cell, G_{ads} is the solid-fluid interaction parameter, R is the bubble radius, and Δp is the Laplace pressure.

n_s	G_{ads}	R (m)	Δp (Pa)	γ (N/m)
0.0	0.0	1.487E-05	2782.64	0.04137
0.4	0.0	1.487E-05	2847.24	0.04234
0.4	0.2	1.487E-05	2847.24	0.04234
0.4	0.4	1.487E-05	2847.24	0.04234
0.5	0.0	1.488E-05	2842.64	0.04230
0.5	0.2	1.488E-05	2842.64	0.04230
0.5	0.4	1.488E-05	2842.64	0.04230
0.6	0.0	1.488E-05	2838.23	0.04222
0.6	0.2	1.488E-05	2838.23	0.04222
0.6	0.4	1.488E-05	2838.23	0.04222
0.9	0.0	1.488E-05	2804.23	0.04174

fully absorbed into the solid. Therefore, the effect of the homogenized model on the contact angle was studied using an approach similar to the Washburn experiment [15]. A tube or channel is filled in equal parts with electrolyte and gas, where the electrolyte is absorbed into the channel by attractive solid-fluid interaction forces. The speed of the absorption, i.e. the velocity of the advancing electrolyte-gas interface $v_x = \mathrm{d}\mathbf{x}/\mathrm{d}t$ correlates with G_{ads}.

This correlation can be derived from Hagen-Poiseuille's law for a capillary with radius R_{pore} and the capillary pressure $\Delta p = 2\gamma\cos(\theta)/R_{\text{pore}}$:

$$\begin{aligned} \frac{\mathrm{d}V}{\mathrm{d}t} = \frac{\mathrm{d}\mathbf{x}(\pi R_{\text{pore}}^2)}{\mathrm{d}t} &= \frac{\pi R_{\text{pore}}^4 \Delta p}{8\eta L} \\ v_x = \frac{\mathrm{d}\mathbf{x}}{\mathrm{d}t} &= \frac{R_{\text{pore}}\gamma\cos(\theta)}{4\eta L}. \end{aligned} \tag{SI.7}$$

Here, $\mathrm{d}V/\mathrm{d}t$ is the volumetric flow rate, η is the dynamic viscosity of the electrolyte, and L is the length of the capillary.

The simulation setup consists of a 2D system with a size of $L = 500$ cells along the x- and $H = 5$ cells along the y-direction. Each cell was handled the same way as the

binder in the present paper, i.e. the homogenized model was applied. A constant density was prescribed at boundaries in x-direction, whereas periodic boundary conditions were applied in y-direction. The left and the right half of the system were initialized with an electrolyte with density ρ^{E} and a gas phase with density ρ^{G}, respectively. Both components had equal masses. No pressure gradient or other external force field was applied. The model parameters were similar to those given in Table 1 in the present paper.

A simulation run consisted of 1,500,000 time steps. Due to the attractive adhesive forces on the electrolyte, the interface started moving along the $+x$-direction, i.e. electrolyte displacing gas. The interface velocity v was determined every 10,000 time steps.

The solid fraction n_s was varied in the range $n_s = [0.3, 0.7]$. This range includes the values of n_s that were chosen in the present paper. For each value of n_s, a broad range of values for $G_{\mathrm{ads}} = G^{\mathrm{G}}_{\mathrm{ads}} = -G^{\mathrm{E}}_{\mathrm{ads}}$ was considered and the velocity of the advancing electrolyte-gas interface v was recorded. The contact angle θ was then determined by inserting v into Eq. (SI.7). The corresponding results of θ are given in Table SI-2. They indicate that the contact angle mainly depends on G_{ads} and is hardly affected by n_s. However, n_s correlates with the capillary radius R_{pore} in the range between $R = 132\,\mathrm{nm}$ and $R = 290\,\mathrm{nm}$ which agrees with experimental values from the literature [16].

Table SI-2: Results of the contact angle θ determined from the capillary simulations. The parameter n_s is the solid fraction of the homogenized lattice cell, R_{pore} is the capillary radius, and G_{ads} is the solid-fluid interaction parameter.

n_s	R_{pore} (nm)	$G_{\mathrm{ads}} =$	0.05	0.10	0.15	0.175	0.20	0.25	0.30	0.32
0.3	290	θ (°) =	81.96	73.36	64.28	63.66	54.41	45.05	29.14	19.57
0.4	248		81.75	73.12	64.18	59.49	54.48	42.85	29.04	22.15
0.5	220		82.06	73.80	65.17	60.64	55.68	44.32	29.27	20.39
0.6	180		82.11	73.96	65.37	60.80	55.92	44.79	29.80	20.97
0.7	132		82.11	73.96	65.37	60.80	55.92	44.79	29.80	20.97

The values of G_{ads} that were chosen for this study were taken from Table SI-2. In particular, we used $G_{\mathrm{ads}} = \{0.3, 0.175, 0.0, -0.175\}$ for the corresponding binder contact angles $\theta_{\mathrm{B}} = \{30, 60, 90, 120\}°$.

SI-3. Uncertainty Estimation for Pressure-Saturation Behavior

Filling simulations were conducted for five different, statistically equivalent electrode realizations which had the same macroscopic electrode properties. All electrode realizations correspond to a medium particle size distribution R_{PS} = medium, the volume fraction of the active material $\phi_{\mathrm{A}} = 0.6$, wettability $\theta_{\mathrm{A}} = 90°$, and no binder content. Separate pressure-saturation curves were determined from each simulation and an average pressure-saturation curve was derived.

The corresponding results of both the separate and the average pressure-saturation curves are shown in Figure SI-2. They are depicted as blue and black solid lines, respectively. The red shaded area shows the confidence band that arises from adding and subtracting the point-wise standard deviation from the average pressure-saturation curve. The results of the different electrode realizations are in good agreement. The mean standard deviation of the average curve is 3.74 kPa over the full range of values, i.e. $S^{\mathrm{E}} = [4,\ 90]\,\%$, including the steep sides, where small shifts in saturation lead to large deviations. For the reduced range, i.e. $S^{\mathrm{E}} = [10,\ 80]\,\%$, where the steep sides are excluded, the mean standard deviation is 2.62 kPa. The average value of the final degree of saturation is $S^{\mathrm{E}}_{\mathrm{final}} = S^{\mathrm{E}}(t_{\mathrm{end}}) = 90.5\,\%$. The corresponding mean standard deviation is 0.75 %.

In addition, by relating each discrete value $p(S^{\mathrm{E}}_i)$ with $i \in \{1, ..., \mathrm{Data}\}$ to the corresponding value of the average pressure-saturation curve, i.e. $\left\langle \Delta p(S^{\mathrm{E}}_i) \right\rangle$, also the bias

$$\mathrm{bias} = \frac{1}{N_{\mathrm{Data}}} \sum_{i=1}^{N_{\mathrm{Data}}} \left(1 - \frac{\Delta p(S^{\mathrm{E}}_i)}{\langle \Delta p(S^{\mathrm{E}}_i) \rangle} \right), \tag{SI.8}$$

the average absolute deviation (AAD)

$$\mathrm{AAD} = \frac{1}{N_{\mathrm{Data}}} \sum_{i=1}^{N_{\mathrm{Data}}} \left| 1 - \frac{\Delta p(S^{\mathrm{E}}_i)}{\langle \Delta p(S^{\mathrm{E}}_i) \rangle} \right|, \tag{SI.9}$$

and the maximum deviation (Δ_{max})

$$\Delta_{\mathrm{max}} = \max_{i=1,\ldots,N_{\mathrm{Data}}} \left(\left| 1 - \frac{\Delta p(S^{\mathrm{E}}_i)}{\langle \Delta p(S^{\mathrm{E}}_i) \rangle} \right| \right) \tag{SI.10}$$

were determined. The values are given in Table SI-3.

Regarding Table SI-3 the AADs of all samples show a good agreement with the average pressure-saturation curve. The best agreement was observed for the electrode realization 4.

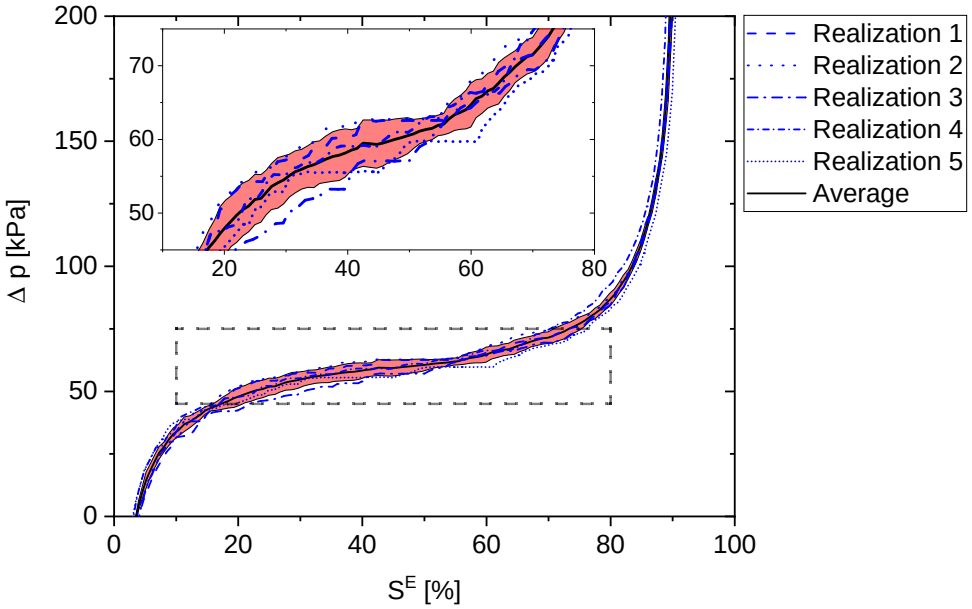

Figure SI-2: Comparison of pressure-saturation curves determined from filling simulations of five different electrode realizations with similar macroscopic electrode properties (R_{PS} = medium, $\phi_{\mathrm{A}} = 0.6$, $\theta_{\mathrm{A}} = 90°$, no binder content). The corresponding results are shown by the blue lines. The average pressure-saturation curve is shown by the black solid line. The red shaded area shows the confidence band. For a better overview, the section of the figure which is indicated by the dashed gray frame is enlarged and shown at the top.

Table SI-3: Determination of the numerical uncertainty of pressure-saturation curves. Results for five different structural realizations with the same macroscopic electrode parameters were compared. The statistical evaluation is given by the AAD, bias, and maximum deviation. Two sets of comparisons are shown. One spanning the full range of data points, i.e. $S^{\mathrm{E}} = [4,\ 90]\,\%$, and another spanning a reduced range, i.e. $S^{\mathrm{E}} = [10,\ 80]\,\%$. The mean standard deviations for the full and the reduced range are 3.74 kPa and 2.62 kPa, respectively.

	data range	N_{Data}	bias (%)	AAD (%)	$\Delta_{\max}$ (%)
realization 1	$S^{\mathrm{E}} = [4,\ 90]\,\%$	104	-0.75	3.89	23.35
	$S^{\mathrm{E}} = [10,\ 80]\,\%$	76	-1.86	3.11	12.29
realization 2	$S^{\mathrm{E}} = [4,\ 90]\,\%$	104	-3.01	5.99	52.18
	$S^{\mathrm{E}} = [10,\ 80]\,\%$	76	-4.37	4.64	8.68
realization 3	$S^{\mathrm{E}} = [4,\ 90]\,\%$	105	3.82	4.55	26.69
	$S^{\mathrm{E}} = [10,\ 80]\,\%$	76	4.29	4.49	10.25
realization 4	$S^{\mathrm{E}} = [4,\ 90]\,\%$	105	-1.74	3.12	39.70
	$S^{\mathrm{E}} = [10,\ 80]\,\%$	76	-1.27	1.70	7.39
realization 5	$S^{\mathrm{E}} = [4,\ 90]\,\%$	105	1.64	6.09	87.88
	$S^{\mathrm{E}} = [10,\ 80]\,\%$	76	3.21	3.74	9.34

It was therefore used as a reference and is denoted as default simulation or ID 1 in the present paper.

SI-4. Numerical Simulation Results from the Present Study

The numerical results of the pressure-saturation simulations are summarized in File 1. In addition, the data of the permeabilities k_y^{E} and k_y^{G}, the tortuosities τ_0 and τ_{end}, as well as the electrochemically active surface area $A_{\mathrm{A,act}}$ are given in File 2. All data are provided as *.xls*-files and are attached to the Supporting Information.

File 1: Data set of the pressure-saturation relationships from the present work. Results are sorted by their simulation ID. Beside the simulation time t also the electrolyte saturation $S^{\mathrm{E}}(t)$ and the pressure $\Delta p(t)$ is given. The data are shown in the Figures 2, 3, and 4 in the main paper.
see *PressureSaturation.xls*

File 2: Data set of the of the electrolyte and gas permeabilities k_y^{E} and k_y^{G} as well as their standard deviations. In addition, the data of the geodesic tortuosities τ_0 and τ_{end} as well as the electrochemically active surface area $A_{\mathrm{A,act}}$ are given. The data are shown in Figures 8, 9, and 10 in the main paper.
see *Permeability_ Tortuosity_ ActiveArea.xls*

SI-5. Gas Entrapment

In Section 5.3 of the present paper the gas entrapment at the end of the filling process is discussed. However, the corresponding size distributions of the gas agglomerates are only exemplarily shown for the reference cases ID 1 and ID 9. In Figures SI-3 and SI-4 they are shown for all simulations, i.e. ID $1-16$. The results are given as the ratio of the cumulated gas volume V^{G} to the total pore volume $V^{\mathrm{E+G}}$. They are plotted as a function of the equivalent gas bubble radius $R_{\mathrm{eq}}^{\mathrm{G}}$.

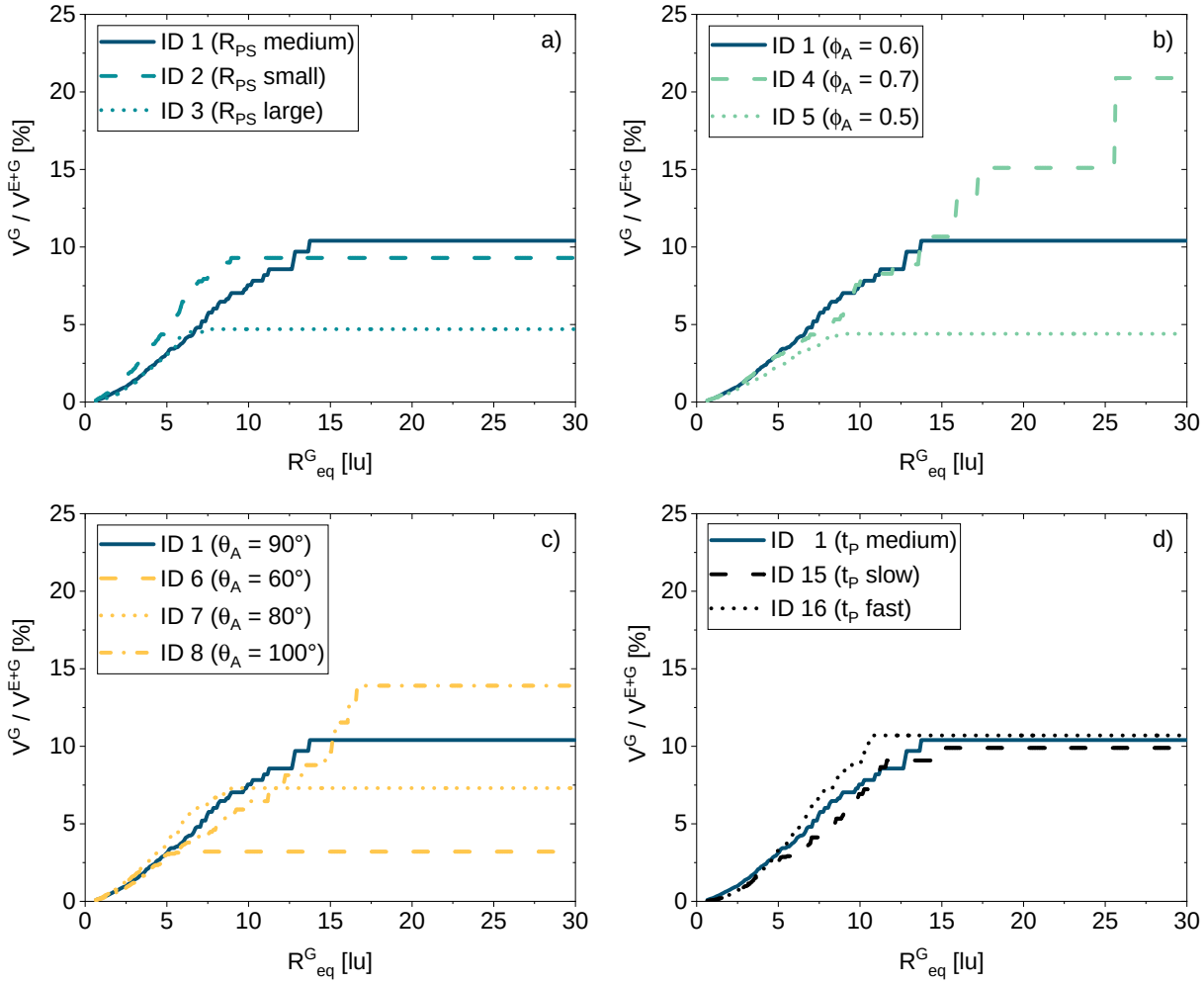

Figure SI-3: Relation between the cumulated gas volume V^{G} divided by the total pore volume $V^{\mathrm{E+G}}$ and the equivalent gas bubble radius $R_{\mathrm{eq}}^{\mathrm{G}}$. Results are shown for the IDs 1−8 and 15−16. The default simulation, i.e. ID 1, is depicted with the blue solid line. The influencing factors are indicated by the colors. Those are a) the particle size distribution R_{PS} (turquoise), b) the volume fraction of the active material ϕ_{A} (green), c) the wettability θ_{A} (orange), and d) the process time t_{P} (black).

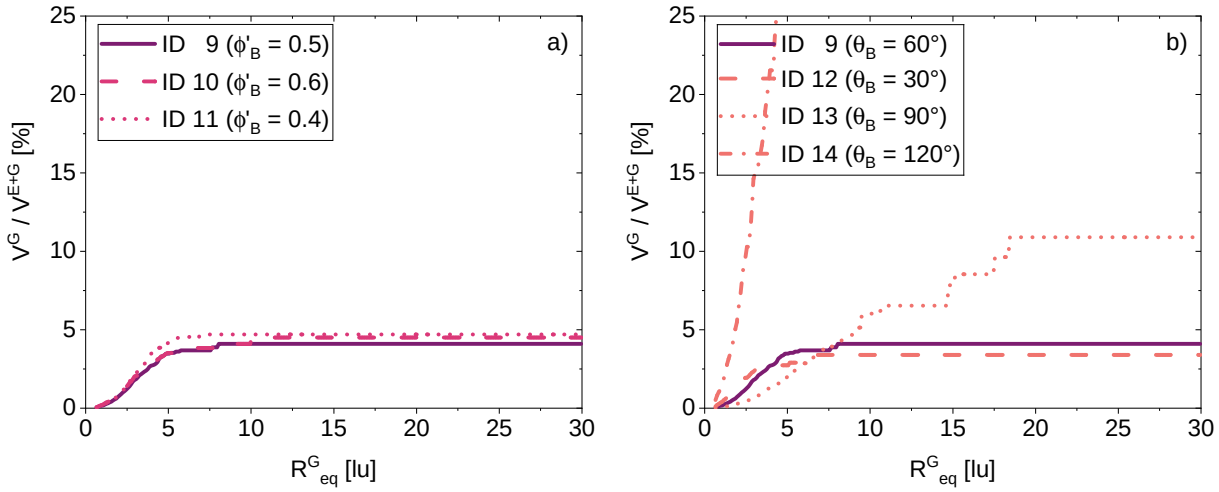

Figure SI-4: Relation between the cumulated gas volume V^{G} divided by the total pore volume $V^{\mathrm{E+G}}$ and the equivalent gas bubble radius $R^{\mathrm{G}}_{\mathrm{eq}}$. Results are shown for the IDs 9−14. The default simulation with binder, i.e. ID 9, is depicted with the purple solid line. The influencing factors are indicated by the colors. Those are a) the inner volume fraction of the binder ϕ'_{B} (magenta), and b) the wettability θ_{B} (red).

References

[1] T. Krueger, H. Kusumaatmaja, A. Kuzmin, O. Shardt, G. Silva, E. Viggen, The Lattice Boltzmann Method: Principles and Practice, Springer, 2016.

[2] P. L. Bhatnagar, E. P. Gross, M. Krook, A model for collision processes in gases. i. small amplitude processes in charged and neutral one-component systems, Physical Review 94 (3) (1954) 511–525. doi:10.1103/PhysRev.94.511.

[3] S. Chen, G. D. Doolen, Lattice Boltzmann method for fluid flows, Annual Review of Fluid Mechanics 30 (1) (1998) 329–364. doi:10.1146/annurev.fluid.30.1.329.

[4] H. Liu, Q. Kang, C. R. Leonardi, S. Schmieschek, A. Narváez, B. D. Jones, J. R. Williams, A. J. Valocchi, J. Harting, Multiphase lattice Boltzmann simulations for porous media applications: A review, Computational Geosciences 20 (4) (2016) 777–805. doi:10.1007/s10596-015-9542-3.

[5] X. Shan, H. Chen, Lattice Boltzmann model for simulating flows with multiple phases and components, Physical Review E 47 (3) (1993) 1815–1819. doi:10.1103/PhysRevE.47.1815.

[6] L. Chen, Q. Kang, Y. Mu, Y. L. He, W. Q. Tao, A critical review of the pseudopotential multiphase lattice Boltzmann model: Methods and applications, International Journal of Heat and Mass Transfer 76 (2014) 210–236. doi:10.1016/j.ijheatmasstransfer.2014.04.032.

[7] C. Pan, M. Hilpert, C. T. Miller, Lattice Boltzmann simulation of two-phase flow in porous media, Water Resources Research 40 (1) (2004) 1–14. doi:10.1029/2003WR002120.

[8] H. Huang, D. T. Thorne, M. G. Schaap, M. C. Sukop, Proposed approximation for contact angles in Shan-and-Chen-type multicomponent multiphase lattice Boltzmann models, Physical Review E 76 (6) (2007) 1–6. doi:10.1103/PhysRevE.76.066701.

[9] Z. Li, S. Galindo-Torres, G. Yan, A. Scheuermann, L. Li, A lattice Boltzmann investigation of steady-state fluid distribution, capillary pressure and relative permeability

of a porous medium: Effects of fluid and geometrical properties, Advances in Water Resources 116 (2018) 153–166. doi:10.1016/j.advwatres.2018.04.009.

[10] D. H. Jeon, Wettability in electrodes and its impact on the performance of lithium-ion batteries, Energy Storage Materials 18 (2019) 139–147. doi:10.1016/j.ensm.2019.01.002.

[11] G. G. Pereira, Fluid flow, relative permeabilities and capillary pressure curves through heterogeneous porous media, Applied Mathematical Modelling 75 (2019) 481–493. doi:10.1016/j.apm.2019.05.050.

[12] A. Shodiev, E. Primo, O. Arcelus, M. Chouchane, M. Osenberg, A. Hilger, I. Manke, J. Li, A. A. Franco, Insight on electrolyte infiltration of lithium ion battery electrodes by means of a new three-dimensional-resolved lattice Boltzmann model, Energy Storage Materials 38 (2021) 80–92. doi:10.1016/j.ensm.2021.02.029.

[13] G. G. Pereira, Grayscale lattice Boltzmann model for multiphase heterogeneous flow through porous media, Physical Review E 93 (6) (2016) 1–14. doi:10.1103/PhysRevE.93.063301.

[14] G. G. Pereira, A multiphase single relaxation time lattice Boltzmann model for heterogeneous porous media, Applied Mathematical Modelling 44 (2017) 160–174. doi:10.1016/j.apm.2016.11.009.

[15] E. W. Washburn, The dynamics of capillary flow, Physical Review 17 (3) (1921) 273–283. doi:10.1103/PhysRev.17.273.

[16] S. R. Daemi, C. Tan, T. Volkenandt, S. J. Cooper, A. Palacios-Padros, J. Cookson, D. J. Brett, P. R. Shearing, Visualizing the carbon binder phase of battery electrodes in three dimensions, ACS Applied Energy Materials 1 (8) (2018) 3702–3710. doi:10.1021/acsaem.8b00501.